$12^{th}$ International Conference on Fracture Mechanics of Concrete and Concrete Structures
FraMCoS-12
B.L.A. Pichler, Ch. Hellmich, P. Preinstorfer (Eds)

https://doi.org/10.21012/FC12.1248
MS08-2:3

# NON-INTRUSIVE STOCHASTIC SBFEM FOR THE UNCERTAINTY QUANTIFICATION OF STRESS INTENSITY FACTORS

**George Litainas[1], Savvas P. Triantafyllou[1], Adrian Egger[2] and Eleni N. Chatzi[3]**

[1] National Technical University of Athens
e-mail: georgelitain@mail.ntua.gr, savtri@mail.ntua.gr

[2]Cubus AG, 8052 Zürich, Switzerland
e-mail: a.egger@cubus.ch

[3]Department of Civil, Environmental and Geomatic Engineering, ETH Zürich, 8093 Zürich, Switzerland
e-mail: chatzi@ibk.baug.ethz.ch

**Key words:** Stress Intensity Factors (SIFs); Scaled Boundary Finite Element Method (SBFEM); Stochastic Fracture

**Abstract.** Predictive modeling of crack initiation is of extreme interest to the engineering community. Within the context of elastic fracture mechanics, the Scaled Boundary Finite Element Method (SBFEM) has proven both efficient and accurate in estimating Stress Intensity Factors (SIFs). More specifically, the SBFEM allows for an analytical evaluation of the stress field as it approaches the crack tip while reducing the dimensionality of the numerical problem by one. In contrast to other methods, e.g., the FEM or the XFEM, no adjustments to the solution procedure are required, and SIFs can be conveniently extracted during post-processing. However, experimental observations on crack initiation are typically underlined by a significant statistical dispersion. This is mainly due to uncertainties arising from the geometry of the crack tip and the variability of the material properties due to e.g., inhomogeneities at the micro or meso-material scale. To this end, this study presents an efficient approach for estimating SIFs under uncertainty. A stochastic scaled boundary finite element method is developed, and the merits and bottlenecks of a non-intrusive implementation are investigated. Furthermore, a comparative study is performed vis-à-vis the discretization method employed to generate sample domains, i.e., the Expansion Optimal Linear Estimation (EOLE) and the Karhunen-Loève Expansion (KL).

## 1 INTRODUCTION

Considering the spatial distribution variability of input variables is of utmost importance to accurately quantify the uncertainty of a system. Fluctuations have a major impact on interpreting how distributions propagate within the domain, with consequences affecting the reliability of a system. Hardly ever does a deterministic solution have the ability to quantify every conceivable situation, as numerous experiments have demonstrated that uncertainties exist in nonhomogeneous material properties and structural topology. As a consequence, random processes are indispensable tools for estimating these fluctuations. Generally, stochastic processes illustrate the actual variance at every location of the discretized geometry using a finite number of variables with a specific mean value and standard deviation, ensuring that the spatial variability of input parameters is accurately represented in the computational analysis. Over the years, many methods have been

developed to introduce random properties in the input parameters [3, 17]. Unambiguously, the Karhunen–Loève expansion (KL) [8, 14, 20] is the flagship of stochastic methods for introducing randomness into a system by decomposing the covariance function using independent standard normal variables. The parameters of KL expansion are calculated via the solution of the Fredholm integral equation, which is an independent problem. Because of the fact that the shapes we deal with are irregular, in most cases, the Fredholm integral equation must be solved numerically [1]. Furthermore, the Expansion Optimal Linear Estimation (EOLE) [11] has acquired a strong reputation for its ability to derive eigenvalues and eigenfunctions regardless of the domain geometry or the covariance function.

Over time, efficient computational tools have been created, such as the Finite Element Method [2], the Virtual Element Method [18], Isogeometric Analysis [6], and the Extended Finite Element Method [10] with the aim of solving numerically integral or partial derivative equations. The Scaled Boundary Finite Element Method (SBFEM) has been added to the arsenal of computational mechanics techniques [15, 16]. In particular, the SBFEM is a powerful asset offering accurate semi-analytical solutions with considerable applications in fracture mechanics, such as the calculation of stress intensity factors (SIFs). The SBFEM, under the assumption of random properties, has been successfully applied in recent years, yielding excellent results. [4] examined the probabilistic fracture mechanics using Monte Carlo simulation, emphasizing the implementation of random fields to model material uncertainties to extract SIFs for tension and shear problems. [5] explores reliability evaluation techniques, including Monte Carlo Simulations (MCS) using first-/second-order reliability methods, emphasizing the SBFEM's accuracy in considering uncertainties without requiring re-meshing. [9] improved hybrid reliability analysis for cracked structures combining probabilistic methods with SBFEM. [12] demonstrates that SBFEM provides high accuracy for reliability analysis and stochastic fracture mechanics with significant computational efficiency with respect to traditional methods. In [7], an efficient method is proposed for handling multiple input uncertainties using (SBFEM) with high computational efficiency and accuracy. In [19], the SBFEM employed NURBS-based Isogeometric Analysis (IGA) reducing computational cost while maintaining high accuracy.

Based on the aforementioned, the SBFEM has proven beneficial in resolving uncertainties with reduced computational costs and increased accuracy. In this work, we further examine the potential benefits of employing quad-tree decompositions to reduce computational times further. The drive is twofold. First, The well known issue of hanging nodes between adjacent blocks of different sizes does not affect SBFEM, since at its core it is a polygon based method. By balancing the quadtree, only a limited amount of possible polygon orientations exist, which can be easily precomputed and retrieved as necessary. Second, quad-tree decompositions are ideal for adaptively resolving domains with features.

To this end, a non-intrusive stochastic scaled boundary finite element method (SSBFEM) is presented. The Young's modulus of the domain is modeled as a random field and two different discretization methods are examined, i.e., the Karhunen–Loève expansion (KL) and the Expansion Optimal Linear Estimation (EOLE). The focal point is the derivation of probability measures for the stress intensity factors SIFs.

This paper is divided into the following sections. The SBFEM theory is briefly presented in Section 2; Section 3 discusses the random field discretization methods considered in this contribution; Section 4 presents the formulation of stochastic SBFEM; in Section 5.1 results are presented with the objective of benchmarking the proposed approach and conclusions are provided in Section 6.

## 2 The scaled boundary finite element method (SBFEM)

The mathematical formulation of the Scaled Boundary Finite Element Method (SBFEM) builds on the definition of a scaled boundary coordinate system (see Fig. 1) with $0 \leq \xi \leq 1$ and $-1 \leq \eta \leq 1$ being the radial and the circumferential coordinates, respectively. In this, $\xi = 0$ corresponds to the scaling center, and $\xi = 1$ corresponds to any point along the element boundary.

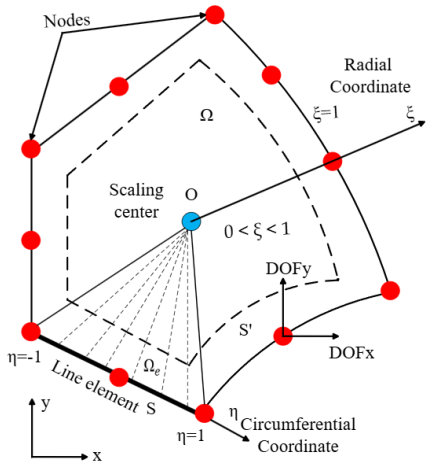


Figure 1: A scaled boundary element with its corresponding scaled coordinates.

The scaling center is defined such that it may be visible from every point on the domain boundary.

### 2.1 Stiffness matrix formulation

The transformation from Cartesian coordinates $(x, y)$ to the scaled boundary coordinates $(\xi,\ \eta)$ along the radial line within each subdomain defined by a boundary element $S^i$ is

$$\begin{aligned} x\left(\xi,\eta\right) &= x_O + \xi x(\eta) = x_O + \xi \boldsymbol{N_u(\eta) x_b^i} \\ y\left(\xi,\eta\right) &= y_O + \xi y(\eta) = y_O + \xi \boldsymbol{N_u(\eta) y_b^i}, \end{aligned} \tag{1}$$

where $x_O, y_O$ are the Cartesian coordinates of the scaling center and $\boldsymbol{x_b^i} = [x_1^i, x_2^i, ..., x_n^i]^T$, $\boldsymbol{y_b^i} = [y_1^i, y_2^i, ..., y_n^i]^T$ correspond to the Cartesian Coordinates of the $n$ nodes of $S^i$. Furthermore, $\boldsymbol{N}_u(\eta) = [N_1(\eta), N_2(\eta), ..., N_n]$ are the boundary element interpolation functions.

In the following, a first order SBFEM formulation is considered, i.e. each boundary element $S^i$ is generated by 2 nodal points. Hence, a linear interpolation scheme is employed and Eq. (1) assumes the following form

$$\begin{aligned} x &= \xi\left(\frac{1}{2}(x_1 + x_2) + \frac{1}{2}(x_2 - x_1)\eta\right) \\ y &= \xi\left(\frac{1}{2}(y_1 + y_2) + \frac{1}{2}(y_2 - y_1)\eta\right) \end{aligned} \tag{2}$$

where $x_O = y_O = 0$ for brevity.

Using the interpolation scheme introduced in Eq. (1), the displacement field is established as

$$\boldsymbol{u}(\xi,\eta) = \boldsymbol{N}_u(\eta)\boldsymbol{u}(\xi). \tag{3}$$

Furthermore, using the strain-displacement compatibility equations, the strains emerge as

$$\boldsymbol{\epsilon}(\xi,\eta) = \boldsymbol{B}_1(\eta)\boldsymbol{u}_{,\xi}(\eta)(\xi) + \frac{1}{\xi}\boldsymbol{B}_2(\eta)\boldsymbol{u}(\xi), \tag{4}$$

where $\boldsymbol{B}_1(\eta)$ and $\boldsymbol{B}_2(\eta)$ are the strain displacement matrices which are defined as:

$$\boldsymbol{B}_1(\eta) = \frac{1}{|\boldsymbol{J}(\eta)|}\begin{bmatrix} \boldsymbol{y}_{b,\eta} & 0 \\ 0 & -\boldsymbol{x}_{b,\eta} \\ -\boldsymbol{x}_{b,\eta} & \boldsymbol{y}_{b,\eta} \end{bmatrix}\boldsymbol{N}_u(\eta) \tag{5}$$

and

$$\boldsymbol{B}_2(\eta) = \frac{1}{|\boldsymbol{J}(\eta)|}\begin{bmatrix} -\boldsymbol{y}_{b,\xi} & 0 \\ 0 & \boldsymbol{x}_{b,\xi} \\ \boldsymbol{x}_{b,\xi} & -\boldsymbol{y}_{b,\xi} \end{bmatrix}\boldsymbol{N}_u(\eta)_{,\eta} \tag{6}$$

respectively, $|\boldsymbol{J}(\eta)|$ is the determinant of the Jacobian, and $\boldsymbol{x}_{,\cdot}$ and $\boldsymbol{y}_{,\cdot}$ denote the partial derivatives of the scaled coordinates in Eq. (1). The determinant is expressed as

$$|J| = x_\eta(\eta)\frac{\partial y_\eta(\eta)}{\partial \eta} - y_\eta(\eta)\frac{x_\eta(\eta)}{\partial \eta}. \tag{7}$$

Finally, the stress field is expressed as

$$\boldsymbol{\sigma}(\xi,\eta) = \boldsymbol{D}\left(\boldsymbol{B}_1(\eta)\boldsymbol{u}(\xi)_{,\xi} + \frac{1}{\xi}\boldsymbol{B}_2(\eta)\boldsymbol{u}(\xi)\right), \tag{8}$$

where $\boldsymbol{D}$ is the elasticity constitutive matrix.

By applying the principle of virtual work to an individual S-element, the scaled boundary finite element equations emerge as

$$\boldsymbol{p} = \boldsymbol{E}_0 \boldsymbol{u}_{,\xi}(\xi) + \boldsymbol{E}_1^T \boldsymbol{u}(\xi) \tag{9}$$

and

$$\begin{aligned} \boldsymbol{E}_0 \xi^2 \boldsymbol{u}_{,\xi\xi}(\xi) + [\boldsymbol{E}_0 + \boldsymbol{E}_1^T - \boldsymbol{E}_1]\xi \boldsymbol{u}_{,\xi}(\xi) \\ - \boldsymbol{E}_2 \boldsymbol{u}(\xi) = \boldsymbol{0}, \end{aligned} \tag{10}$$

where $\boldsymbol{p}$ is the vector of nodal forces. The coefficient matrices $\boldsymbol{E}_0$, $\boldsymbol{E}_1$ and $\boldsymbol{E}_2$ are obtained by assembling element contributions in a direct stiffness fashion according to Eqs. (37), (38), and (40), respectively, i.e.,

$$\boldsymbol{E}_0 = \underset{e}{\mathcal{A}} \int_S \boldsymbol{B}_1^T(\eta) \boldsymbol{D} \boldsymbol{B}_1(\eta) |J| d\boldsymbol{\eta} \tag{11}$$

$$\boldsymbol{E}_1 = \underset{e}{\mathcal{A}} \int_S \boldsymbol{B}_2^T(\eta) \boldsymbol{D} \boldsymbol{B}_1(\eta) |J| d\boldsymbol{\eta} \tag{12}$$

$$\boldsymbol{E}_2 = \underset{e}{\mathcal{A}} \int_S \boldsymbol{B}_2^T(\eta) \boldsymbol{D} \boldsymbol{B}_2(\eta) |J| d\boldsymbol{\eta}, \tag{13}$$

where $\underset{e}{\mathcal{A}}$ denotes the finite element assembly operator over the boundary elements $e$.

The general solution of Eq. (10) assumes the following analytical form

$$\boldsymbol{u}(\xi) = \sum_{i=1}^{n} c_i \xi^{-\lambda_i} \boldsymbol{\phi}_i \tag{14}$$

where $\lambda_i$ correspond to the modal scaling factors in the radial direction, $\boldsymbol{\phi}_i$ are modal displacements, $c_i$ are the integration constants, and $n$ is the total number of degrees of freedom. Substituting Eq. (14) in Eq. (9) and Eq. (10) results in the following eigenvalue problem

$$\boldsymbol{Z}\boldsymbol{\Phi} = \boldsymbol{\Phi}\boldsymbol{\lambda} \tag{15}$$

where

$$\boldsymbol{Z} = \begin{bmatrix} \boldsymbol{E}_0^{-1}\boldsymbol{E}_0^T & -\boldsymbol{E}_0^{-1} \\ \boldsymbol{E}_1\boldsymbol{E}_0^{-1} - \boldsymbol{E}_2 & -\boldsymbol{E}_1\boldsymbol{E}_0^{-1} \end{bmatrix}, \tag{16}$$

is a Hamiltonian matrix of order $2n$.

For a deformable finite domain, the solution to Eq. (15) gives rise to a set of eigenvalues with positive, $\boldsymbol{\lambda}_P$, and negative, $\boldsymbol{\lambda}_N$, real parts. Hence, the system of Eq. (15) assumes the following form:

$$\boldsymbol{Z} \begin{bmatrix} \boldsymbol{\Phi}_{11} & \boldsymbol{\Phi}_{12} \\ \boldsymbol{\Phi}_{21} & \boldsymbol{\Phi}_{22} \end{bmatrix} = \begin{bmatrix} \boldsymbol{\Phi}_{11} & \boldsymbol{\Phi}_{12} \\ \boldsymbol{\Phi}_{21} & \boldsymbol{\Phi}_{22} \end{bmatrix} \begin{bmatrix} \boldsymbol{\lambda}_N & \boldsymbol{0} \\ \boldsymbol{0} & \boldsymbol{\lambda}_P \end{bmatrix}. \tag{17}$$

Therefore, the stiffness matrix of the sub-domain can be evaluated through:

$$\boldsymbol{K}_e = \boldsymbol{\Phi}_{21} \boldsymbol{\Phi}_{11}^{-1} \tag{18}$$

Once the stiffness matrix for the entire domain is constructed, the nodal displacements $\boldsymbol{U}$ are obtained by solving the equilibrium equation, considering the applied constraints and nodal forces.

$$\boldsymbol{P} = \boldsymbol{K}\boldsymbol{U} \tag{19}$$

Where $\boldsymbol{P}$ are the nodal forces on the boundary that are constructed from $\boldsymbol{p}$, see Eq. (9). Upon determining the displacement vector $\boldsymbol{U}$, the integration constant matrix $\boldsymbol{c}$ of each sub-domain can be calculated by:

$$\boldsymbol{c} = \boldsymbol{\Phi}_{11}^{-1} \boldsymbol{U}_e \tag{20}$$

and eventually using Eq. (14) the displacement field of the sub-domain is retrieved

$$\boldsymbol{u}(\xi, \eta) = \boldsymbol{N}^u(\eta) \sum_{i=1}^{n} c_i \xi^{-\lambda_i} \boldsymbol{\phi}_i. \tag{21}$$

Finally, the stress field of each sub-domain is evaluated as:

$$\begin{aligned} \boldsymbol{\sigma}(\xi, \eta) = \boldsymbol{D} \sum_{i=1}^{n} c_i \xi^{-\lambda_i - 1} \\ \big[-\lambda_i \boldsymbol{B}_1(\eta) + \boldsymbol{B}_2(\eta)\big] \boldsymbol{\phi}_i \end{aligned} \tag{22}$$

## 3 Representation of stochastic fields

In order to introduce randomness into material properties, stochastic methods are necessary. After a proper number of realizations, a statistical sample is created at a specific point of the domain, as shown in Fig. 2.

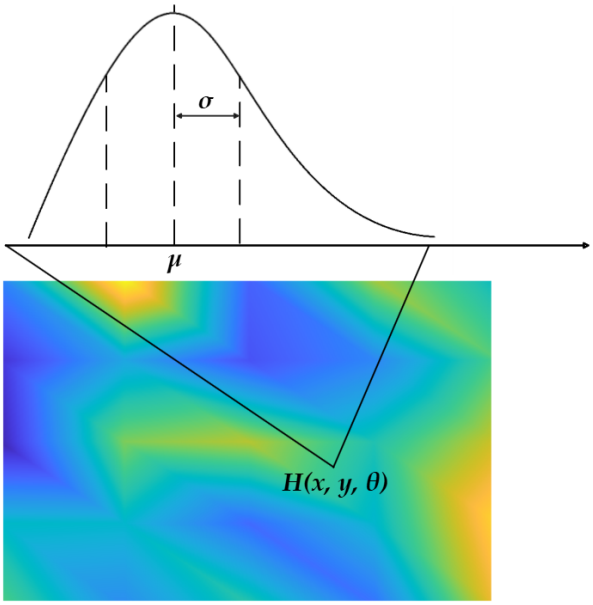


Figure 2: The statistical distribution of a material property from a realization at a single point of the domain $\Omega$ with mean value $\mu$ and standard deviation $\sigma$.

Due to the fact that we deal with mathematical series with an infinite number of random variables and, as a consequence, it is impossible to be applied in the field of computational mechanics. Consequently, the infinite number is replaced by a finite number of random variables without affecting the statistical results. For this reason, the Karhunen–Loève (KL) expansion and Expansion Optimal Linear Estimation methods are formulated with the view to quantifying the convergence standard deviation of the Stress Intensity Factors (SIFs). This section derives these methods assuming the constitutive elastic matrix follows the Gaussian assumption.

### 3.1 The Karhunen–Loève expansion

The truncated Karhunen–Loève (KL) expansion represents a random field $H(\boldsymbol{x}, \theta)$ in terms of its covariance structure. For a given covariance function $\boldsymbol{Cov(x_1, x_2)}$, the KL expansion is formulated as:

$$H(\boldsymbol{x}, \theta) = \mu_H(\boldsymbol{x}) + \sigma_H(\boldsymbol{x}) \sum_{i=1}^{\infty} \sqrt{\lambda_i} \phi_i(\boldsymbol{x}) \xi_i(\boldsymbol{\theta}), \tag{23}$$

where $\mu_H(\boldsymbol{x})$ and $\sigma_H(\boldsymbol{x})$ are the mean and standard deviation of the random field, respectively, $\{\xi_\theta, i = 1, 2, 3, ...\}$ is a finite set of independent standard normal variables, and $\lambda_i$, $\phi_i(\boldsymbol{x})$ are the $i^{th}$ eigenvalue and eigenfunction, respectively, which emerge via the solution of the following Fredholm integral equation

$$\int_{\Omega_{x'}} Cov(\boldsymbol{x}, \boldsymbol{x'}) \phi_i(\boldsymbol{x'}) d\boldsymbol{\Omega}_{\boldsymbol{x'}} = \lambda_i \phi_i(\boldsymbol{x}). \tag{24}$$

In Eq. (24), $\Omega_{x'}$ is the domain, $\boldsymbol{x}$, $\boldsymbol{x'}$ are the spatial coordinates, and $\mathrm{Cov}(\boldsymbol{x}, \boldsymbol{x'})$ is the autocorrelation function defined as

$$Cov(\boldsymbol{x}, \boldsymbol{x'}) = \sigma(\boldsymbol{x}) \cdot \sigma(\boldsymbol{x'}) \cdot \rho(\boldsymbol{x}, \boldsymbol{x'}) \tag{25}$$

with $\rho(\boldsymbol{x}, \boldsymbol{x'})$ the autocorrelation coefficient function.

For random fields with arbitrary autocorrelation functions in complex geometries, the eigen solutions of the Fredholm equation must be solved numerically [13]. Under these conditions, the Galerkin method is applied using, e.g., the finite element framework. For a given autocorrelation function, each eigenfunction can be efficiently represented as a series expansion over the chosen basis, expressed as:

$$\phi_j(\boldsymbol{x}) = \sum_{k=1}^{N} d_{jk} h_k(\boldsymbol{x}) \tag{26}$$

where $N$ is the number of nodes in the discretized geometry. Using Eq. (26) in Eq. (24) and projecting the eigenfunctions onto the space of the shape functions $\mathcal{H}_N$, ensuring that the truncated series serves as the projection is orthogonal in $\mathcal{L}(\Omega)^2$, the final form of Eq. (24) is reformulated as:

$$\sum_{i=1}^{N} \Bigg[ \int_{\Omega_x} \int_{\Omega_{x'}} C_{HH}(\boldsymbol{x}, \boldsymbol{x'}) h_i(\boldsymbol{x}) h_j(\boldsymbol{x'}) d\boldsymbol{\Omega}_{\boldsymbol{x}} d\boldsymbol{\Omega}_{\boldsymbol{x'}} - \lambda_k \int_{\Omega_x} h_i(\boldsymbol{x}) h_j(\boldsymbol{x}) d\boldsymbol{\Omega}_{\boldsymbol{x}} \Bigg] d_i^k = 0 \tag{27}$$

where $\mathcal{L}(\Omega)^2$ is a Hilbert space of square-integrable functions over $\Omega_{\boldsymbol{x}}$ and $\Omega_{\boldsymbol{x'}}$ respectively. The matrix form of Eq. (27) is expressed

as a linear system given by:

$$\boldsymbol{CD} = \boldsymbol{\Lambda BD} \tag{28}$$

Where the matrices $\boldsymbol{C}$, $\boldsymbol{B}$, $\boldsymbol{D}$ and $\boldsymbol{\Lambda}$ of Eq. (28) are N order matrices whose elements are determined by the following equations Eq. (29), Eq. (30), Eq. (31) and Eq. (32) in their respective order:

$$\boldsymbol{C}_{ij} = \int_{\Omega_x}\int_{\Omega_{x'}} Cov(\boldsymbol{x}, \boldsymbol{x'}) h_i(\boldsymbol{x}) h_j(\boldsymbol{x'}) d\boldsymbol{\Omega}_{\boldsymbol{x}} d\boldsymbol{\Omega}_{\boldsymbol{x'}} \tag{29}$$

$$\boldsymbol{B}_{ij} = \int_{\Omega_x} h_i(\boldsymbol{x}) h_j(\boldsymbol{x}) d\boldsymbol{\Omega}_{\boldsymbol{x}} \tag{30}$$

$$\boldsymbol{D}_{ij} = d_{ij} \tag{31}$$

$$\boldsymbol{\Lambda}_{ij} = \delta_{ij}\lambda_j \tag{32}$$

Where $\boldsymbol{D}$ and $\boldsymbol{\Lambda}$ are the eigenvectors and the eigenvalues of Eq. (28) using Gauss quadrature rule for the integrals of Eq. (29) and Eq. (30). Taking into account that $\{\boldsymbol{C}_{ij}, \boldsymbol{D}_{ij}\} \in \mathbb{R}^d$ where $d = \{1, 2, 3\}$, the number integrals of $\boldsymbol{C}, \boldsymbol{D}$ are $2d$ and $d$ respectively.

After solving Eq. (28), the Eq. (33) is truncated after $M$ terms, yielding its final form:

$$H(\boldsymbol{x}, \theta) = \mu_H(\boldsymbol{x}) + \sigma_H(\boldsymbol{x}) \sum_{i=1}^{M} \sqrt{\lambda_i}\phi_i(\boldsymbol{x})\xi_i(\boldsymbol{\theta}) \tag{33}$$

### 3.2 The EOLE method

Notwithstanding that the Fredholm integral Eq. (24) is inherently computationally intensive, especially for a large number of elements, the Expansion Optimal Linear Estimation (EOLE) only requires discretization of the geometry along with the values of the autocorrelation function $\boldsymbol{C}$ at each node of the grid. Accordingly, for a given covariance function with regard to a homogeneous Gaussian field, after truncating to $M$ terms, the random field is established by:

$$H(\boldsymbol{x}, \boldsymbol{\theta}) = \mu_H(\boldsymbol{x}) + \sigma_H(\boldsymbol{x}) \sum_{i=1}^{M} \frac{\xi_i(\theta)}{\sqrt{\lambda_i}} \boldsymbol{\phi_i}^T \boldsymbol{C}_{x_i, x_j} \tag{34}$$

again $\mu_H(\boldsymbol{x})$ and $\sigma_H(\boldsymbol{x})$ represent the mean and standard deviation of Eq. (34) respectively; $\xi_i(\theta)$ is a Gaussian random variable that follows the normal distribution $\mathcal{N} \sim (0, 1)$ and $\lambda_i$ and $\phi_i(\boldsymbol{x})$ are the $i^{th}$ eigenvalue and eigenvector respectively. In this setting, $\lambda_i$ and $\phi_i(\boldsymbol{x})$ emerge as the solution of the following

$$\boldsymbol{C\phi_i} = \lambda_i \boldsymbol{\phi_i}, \tag{35}$$

which contrary to the KL case only requires the evaluation of the covariance matrix $\boldsymbol{C}$ at the nodal points of the discretized domain.

## 4 Stochastic formulation of the scaled boundary finite element method

The stochastic scaled boundary finite element method is a mathematical approach that encompasses randomness to material properties and external forces. In the following, Young's modulus $E$ is modeled as a random field, i.e., $E = H(\boldsymbol{x}, \theta)$, where $\theta$ represents a random event. Consequently, the system's response, e.g., the displacement vector, becomes $\boldsymbol{U} = \boldsymbol{U}(\theta)$.

### 4.1 Formulation of the stochastic scaled boundary finite element method

Using the stochastic SBFEM, the discretization of the random field is made via the Eq. (33) and (34).

To introduce randomness into material properties, under the assumption that the modulus of elasticity follows the Gaussian distribution and utilizing Eq. (33) or (34), the elasticity matrix at a specific point $\boldsymbol{x}$ can be expressed as:

$$\boldsymbol{D}(\boldsymbol{x}, \theta) = H(\boldsymbol{x}, \theta)\boldsymbol{D}_0 \tag{36}$$

where $\boldsymbol{D}_0$ is the constant elastic matrix. Embedding (36) into the coefficient matrices Eq. (37), Eq. (38) and Eq. (40) become redefined as:

$$\boldsymbol{E}_0(\theta) = \underset{e}{\mathcal{A}} \int_S H(\boldsymbol{x}, \theta) \boldsymbol{B}_1^T(\eta) \boldsymbol{D}_0 \boldsymbol{B}_1(\eta) |J| d\boldsymbol{\eta} \tag{37}$$

$$\boldsymbol{E}_1(\theta) = \underset{e}{\mathcal{A}} \int_S H(\boldsymbol{x}, \theta) \boldsymbol{B}_2^T(\eta) \boldsymbol{D}_0 \boldsymbol{B}_1(\eta) |J| d\boldsymbol{\eta} \tag{38}$$

$$\boldsymbol{E}_2(\theta) = \underset{e}{\mathcal{A}} \int_S H(\boldsymbol{x},\theta)\boldsymbol{B}_2^T(\eta)\boldsymbol{D}_0\boldsymbol{B}_2(\eta)|J|d\boldsymbol{\eta} \tag{39}$$

where quantity $\theta$ denotes that Eq. (37), Eq. (38) and Eq. (40) are random variables. Hence Eq. (15) has the final form:

$$\boldsymbol{Z}(\boldsymbol{\theta})\boldsymbol{\Phi}(\boldsymbol{\theta}) = \boldsymbol{\Phi}(\boldsymbol{\theta})\boldsymbol{\lambda}(\boldsymbol{\theta}) \tag{40}$$

Accordingly, the stiffness matrix of each boundary element can be represented in its final form as:

$$\boldsymbol{K}_e(\theta) = \boldsymbol{\Phi}_{21}(\theta)\boldsymbol{\Phi}_{11}^{-1}(\theta). \tag{41}$$

Furthermore, after assembling $\boldsymbol{K}_e(\theta)$ for every realization for each sub-domain, the displacement field $\boldsymbol{U}(\boldsymbol{\theta})$ can be found via the equilibrium equation. The new form of Eq. (19) is:

$$\boldsymbol{K}(\theta)\boldsymbol{U}(\theta) = \boldsymbol{p}. \tag{42}$$

In summary, for each realization $\theta$, the equilibrium equation Eq. (42) is solved to derive the statistical characteristics of displacement field $\boldsymbol{U}(\theta)$. In consequence of this, the equations Eq. (43), Eq. (44), and Eq. (46) will also be stochastic as a result of Eq. (36). Finally, it is obvious that the key to creating stochastic scaled boundary finite elements is to introduce uncertainties into the matrices Eq. (37), Eq. (38), Eq. (40).

### 4.2 Stochastic Stress Intensity factors

One of the most valuable benefits of SBFEM is its application to linear stochastic fracture mechanics under the assumption of random material properties. The primary means of SBFEM are the semi-analytical solutions for displacements extending to stresses and strains in the radial direction, as shown in Fig. 3.

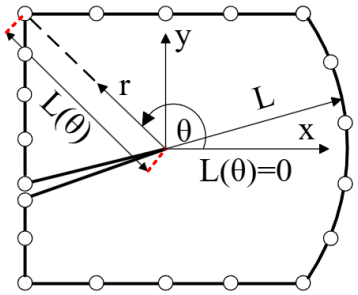


Figure 3: Scaled boundary element for a cracked domain with the scaling center positioned at the crack tip.

Moreover, these mathematical expressions take the form corresponding to each realization.

$$\boldsymbol{c}(\theta) = \boldsymbol{\Phi}_{11}^{-1}(\theta)\boldsymbol{U}_e(\theta) \tag{43}$$

with the integration constant determined, the displacement field of the sub-domain is calculated as:

$$\boldsymbol{u}(\xi,\eta)(\theta) = \boldsymbol{N}^u(\eta)\sum_{i=1}^{n} c_i(\theta)\xi^{-\lambda_i}\boldsymbol{\phi}_i(\theta). \tag{44}$$

Finally, the stress field of each sub-domain is evaluated as:

$$\boldsymbol{\sigma}(\xi,\eta)(\theta) = \sum_{i=1}^{n} c_i(\theta)\xi^{-\lambda_i-1}\boldsymbol{\Phi}_i^{\sigma}(\theta) \tag{45}$$

where $\boldsymbol{\Phi}_i^{\sigma}$ symbolizes the stress modes:

$$\boldsymbol{\Phi}_{\boldsymbol{i}}^{\boldsymbol{\sigma}}(\boldsymbol{\theta}) = \boldsymbol{D}(\boldsymbol{x},\boldsymbol{\theta})\big[-\lambda_i\boldsymbol{B}_1(\eta) + \boldsymbol{B}_2(\eta)\big]\boldsymbol{\phi}_i(\theta) \tag{46}$$

where $\boldsymbol{D}(\boldsymbol{x},\boldsymbol{\theta})$ and $\boldsymbol{\phi}_i(\theta)$ correspond to the stochastic field of the elasticity tensor Eq. (36) and the displacement modes, respectively. The solution of Eq. (15) corresponds to 2N eigenvalues $\boldsymbol{\lambda}_i$. Consequently, the eigenvalues within the range $-1 < \lambda < 0$ account for evaluating fracture modes. Owing to this, the SIFs can be estimated in the following way:

$$\begin{Bmatrix} \boldsymbol{K}_I(\theta) \\ \boldsymbol{K}_{II}(\theta) \end{Bmatrix} = \sqrt{2\pi L}\begin{Bmatrix} \sum_{i=I,II} c_i(\theta)\{\Phi_{yy}^{\sigma}\} \\ \sum_{i=I,II} c_i(\theta)\{\Phi_{xy}^{\sigma}\} \end{Bmatrix} \tag{47}$$

where $L$ is the distance between the crack tip's end and its quad-tree's boundary.

## 5 Applications

In this section, the stochastic evaluation of Stress Intensity Factors (SIFs) is developed under the assumption of input random material fields, as outlined in the previous sections. The main objective of the next three problems is to quantify the standard deviation of the (SIFs) with respect to the orders of the KL and EOLE expansions. The SIFs are evaluated using MCS with 3000 realizations. The covariance function for all cases is assumed to be exponential, i.e.,

$$Cov(\boldsymbol{x},\boldsymbol{y}) = exp\Big(-|\frac{x_1-x_2}{L_x}| - |\frac{y_1-y_2}{L_y}|\Big) \tag{48}$$

where $L_x$ and $L_y$ denote the correlation lengths along the x and y axes respectively. All cases were run using an in-house code developed in MATLAB 2024a on a PC fitted with an Intel Core i7-12800HX and 32 GB of RAM.

### 5.1 Square plate with edge crack

The rectangular plate shown in Fig. 4 is considered with dimensions $L = 1$ and $W = 1$ units. The plate is fixed at the bottom and cracked at mid-height with a crack length $a = 0.5$ units. Furthermore, it is subjected to a tensile pressure $\sigma = 1$ unit, also shown in the figure. A quad-tree mesh comprising 1058 polygons and 1510 nodes is employed.

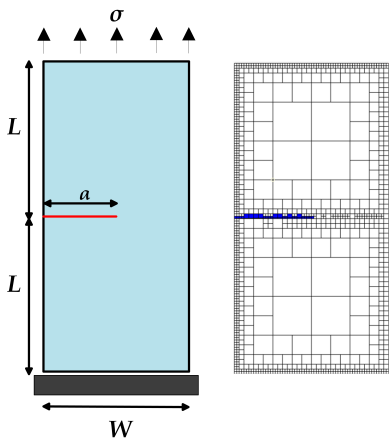


Figure 4: Rectangular plate with a straight crack under tension (left) geometry and boundary conditions (right) quad-tree SBFEM mesh.

The Young's modulus of the plate is assumed to be a Gaussian random field with mean value and standard deviation equal to $\mu_H = 20.7 \cdot 10^6$ and $\sigma_H = 0.2\mu_H$ respectively; the Poisson's ratio is 0.3. Both the KL and EOLE methods are used. To examine the sensitivity of the extracted SIF statistics on the expansion method employed, a series of analyses is performed varying the number of terms considered in the KL and EOLE methods and the correlation lengths.

The standard deviation of the mode-I stress intensity factor, $K_I$, is shown in Fig. 5 as a function of the number of terms $M$ considered in the expansion. For every sample, the fluctuation of Young's modulus is changing. Consequently, the differing distributions with respect to samples affect the resulting Stress Intensity Factors (SIFs). Hence, the standard deviation for every expansion order varies, as is shown in Fig. 5. Both the KL and the EOLE provide converged results for $M \geq 17$. Moreover, the mean values and standard deviations of the first fracture mode $K_I$ using 17 expansion orders for KL and EOLE are shown in Table. 1 and Table. 2 for each correlation length respectively.

The computational cost to compute the distribution of the Stress Intensity Factors (SIFs) using a quad-tree mesh was 4.75 minutes, compared to 36.12 minutes required for a finely meshed domain with 8192 scaled boundary finite elements and 8451 nodes.

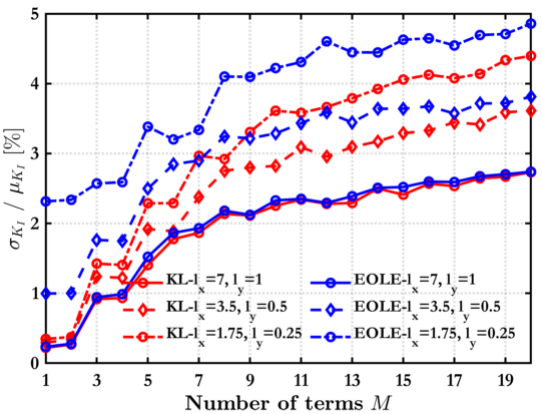


Figure 5: The influence of expansion orders on the standard deviations of $K_I(\theta)$.

Table 1: The mean values of the $K_I$.

| Corelation Lengths | KL | EOLE |
|---|---|---|
| $l_x = 7.0, l_y = 1.0$ | 4.1770 | 4.1768 |
| $l_x = 3.5, l_y = 0.5$ | 4.2246 | 4.2186 |
| $l_x = 1.75, l_y = 0.25$ | 4.2280 | 4.2151 |

Table 2: The standard deviations of the $K_I$.

| Corelation Lengths | KL | EOLE |
|---|---|---|
| $l_x = 7.0, l_y = 1.0$ | 0.1058 | 0.1082 |
| $l_x = 3.5, l_y = 0.5$ | 0.1456 | 0.1507 |
| $l_x = 1.75, l_y = 0.25$ | 0.1724 | 0.1916 |

### 5.2 Square plate with inclined edge crack

Herein, the same tension problem is examined, but the crack is inclined as shown in Fig. 6 with dimensions $a = 0.5$ and $z = 0.5$ units. The rectangular plate is discretized using again a quad-tree mesh consisting of 1058 polygons and 1510 nodes. The Young's modulus of E is simulated as a Gaussian field with mean $\mu_H = 20.7 \cdot 10^6$ and standard deviation and $\sigma_H = 0.1\mu_H$ units, respectively. The Poisson ratio is equal to 0.3 and the tensile pressure $\sigma = 1$ unit.

Similarly to the previous case, the converged standard deviation is obtained for at least 17 expansion orders M as shown in Fig. 7 and 8 for $K_I$ and $K_{II}$, respectively. For this example, since the crack is inclined, the second stochastic fracture mode becomes evident. In that case, the mean values and standard deviations of the first fracture mode $K_I$ using $M = 17$ expansion orders are shown in Table. 3 and Table. 4 while the second fracture mode $K_{II}$ in Table. 5 and Table. 6 for each correlation length and method respectively.

The computational cost to compute the distribution of the Stress Intensity Factors (SIFs) using a quad-tree mesh was 4.76 minutes, as opposed to 38.12 minutes required for a finely meshed domain with 8192 scaled boundary finite elements and 8515 nodes.

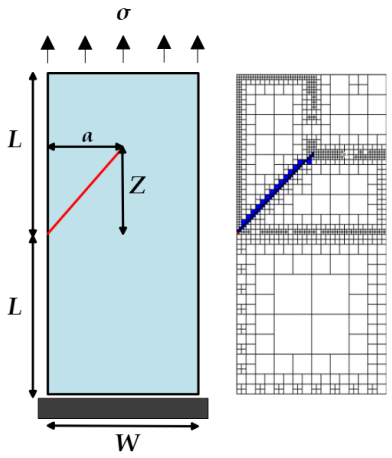


Figure 6: Rectangular plate with an inclined crack under tension (left) geometry and boundary conditions (right) quad-tree SBFEM mesh.

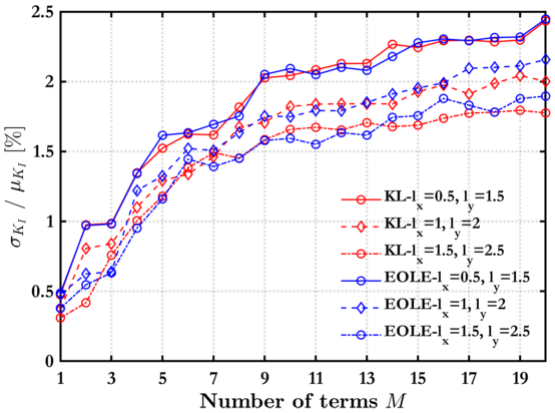


Figure 7: The influence of expansion orders on the standard deviations of $K_I(\theta)$.

Table 3: The mean values of the $K_I$.

| Corelation Lengths | KL | EOLE |
|---|---|---|
| $l_x = 0.5, l_y = 1.5$ | 2.9429 | 2.9425 |
| $l_x = 1.0, l_y = 2.0$ | 2.9227 | 2.9214 |
| $l_x = 1.5, l_y = 2.5$ | 2.9218 | 2.9223 |

Table 4: The standard deviations of the $K_I$.

| Corelation Lengths | KL | EOLE |
|---|---|---|
| $l_x = 0.5, l_y = 1.5$ | 0.0676 | 0.0674 |
| $l_x = 1.0, l_y = 2.0$ | 0.0559 | 0.0612 |
| $l_x = 1.5, l_y = 2.5$ | 0.0518 | 0.0535 |

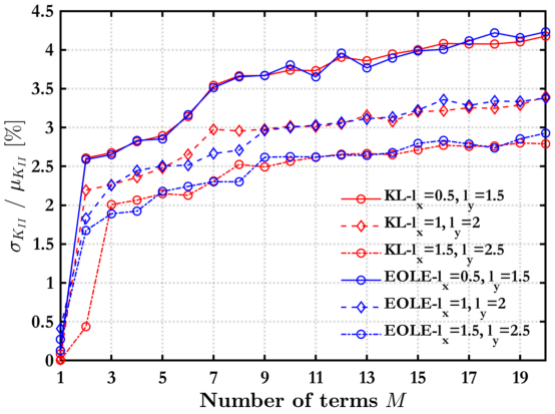


Figure 8: The influence of expansion orders on the standard deviations of $K_{II}(\theta)$.

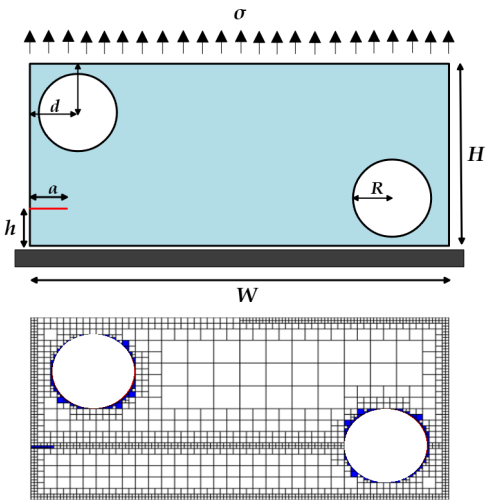


Figure 9: Rectangular plate with two holes and a straight crack (top) Geometry and boundary conditions (bottom) quad-tree SBFEM mesh.

Table 5: The mean values of the $K_{II}$.

| Corelation Lengths | KL | EOLE |
|---|---|---|
| $l_x = 0.5, l_y = 1.5$ | 1.3246 | 1.3241 |
| $l_x = 1.0, l_y = 2.0$ | 1.3241 | 1.3236 |
| $l_x = 1.5, l_y = 2.5$ | 1.3235 | 1.3237 |

Table 6: The standard deviations of the $K_{II}$.

| Corelation Lengths | KL | EOLE |
|---|---|---|
| $l_x = 0.5, l_y = 1.5$ | 0.0540 | 0.0545 |
| $l_x = 1.0, l_y = 2.0$ | 0.0431 | 0.0435 |
| $l_x = 1.5, l_y = 2.5$ | 0.0365 | 0.0369 |

### 5.3 Square plate with two holes and a straight crack

The final example is addressed to a rectangular plate with two holes and a straight crack, whose distance from the bottom is $h = 2.85$ mm. The length of the two cracks is $\alpha = 1$ mm. The radius of the two holes is the same and equal to $R = 2$ mm, while the center of each hole has a distance $d = 3$ mm from the upper and lower boundaries of the plate, as shown in Fig. 9.

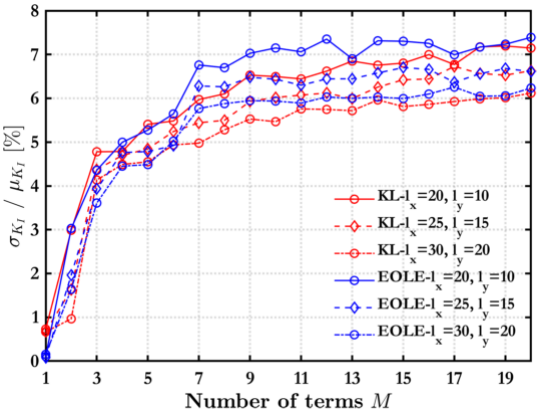


Figure 10: The influence of expansion orders on the standard deviations of $K_I(\theta)$.

The Young's modulus $E$ of the plate is considered to be a Gaussian random field with mean value and standard deviation equal to $\mu = 200$ GPa and $\sigma = 20$ GPa, respectively. Poisson's ratio $\nu = 0.3$ while the tensile pressure is equal to $\sigma = 1$ GPa. The quad-tree mesh here is 1731 polygons and 2321 nodes, as shown in Fig. 9 (bottom).

The standard deviation of $\boldsymbol{K}_I$ varies with the number of $M$ - expansion orders up to 20 as illustrated in Fig. 10. To conclude, the computational cost for 3000 samples was 10.52 minutes using a quad-tree mesh. Finally, the mean values and standard deviations of the first fracture

mode $K_I$ using $M = 17$ expansion orders for KL and EOLE are shown in Table. 7 and Table. 8 respectively.

Table 7: The mean values of the $K_I$.

| Corelation Lengths (mm) | KL | EOLE |
|---|---|---|
| $l_x = 20, l_y = 10$ | 2.0056 | 2.0051 |
| $l_x = 25, l_y = 15$ | 2.0043 | 2.0040 |
| $l_x = 30, l_y = 20$ | 2.0066 | 2.0081 |

Table 8: The standard deviations of the $K_I$.

| Corelation Lengths (mm) | KL | EOLE |
|---|---|---|
| $l_x = 20, l_y = 10$ | 0.1358 | 0.1402 |
| $l_x = 25, l_y = 15$ | 0.1349 | 0.1276 |
| $l_x = 30, l_y = 20$ | 0.1189 | 0.1254 |

## 6 Conclusions

This paper investigates the application of the Scaled Boundary Finite Element Method (SBFEM) over quad-tree meshes within the context of linear stochastic fracture mechanics, assuming random material properties. The constitutive relationship of SBFEM is modeled as a stochastic field employing the KL expansion and the EOLE.

The first and second examples focus on a classical tension problem with a rectangular domain, including a straight and an inclined crack, respectively. The third example involves a non-rectangular domain, where the numerical solution of Stress Intensity Factors (SIFs) is mandatory. By employing various terms in stochastic fields, the semi-analytical solutions provided by SBFEM can accurately estimate both the mean value and standard deviation for each fracture mode. Unfortunately, not only were the KL orders relatively high, but the same orders were used in the EOLE expansion. As a result, intrusive methods cannot be effectively applied in this paper owing to the immense augmented stiffness matrix. The non-intrusive method employed in this work can demonstrate further gains by parallelizing the Monte Carlo runs. As a future outlook, this method can be extended using an intrusive method called the Spectral Stochastic Method in combination with surrogate models to further reduce the computational cost.

## 7 Acknowledgements

The research project is implemented in the framework of H.F.R.I called “Basic research Financing (Horizontal support of all Sciences)” under the National Recovery and Resilience Plan “Greece 2.0” funded by the European Union–NextGenerationEU (H.F.R.I. Project Number: 15097)

## References

[1] A. Basmaji, M. M. Dannert, F. Bensel, R. Fleury, A. Fau, and U. Nackenhorst. Karhunen-loève expansion based on an analytical solution over a bounding box domain. *Probabilistic Engineering Mechanics*, 74:103519, 2023.

[2] K.-J. Bathe. *Finite element procedures*. Klaus-Jurgen Bathe, 2006.

[3] W. Betz, I. Papaioannou, and D. Straub. Numerical methods for the discretization of random fields by means of the karhunen–loève expansion. *Computer Methods in Applied Mechanics and Engineering*, 271:109–129, 2014.

[4] M. S. Chowdhury, C. Song, and W. Gao. Probabilistic fracture mechanics by using monte carlo simulation and the scaled boundary finite element method. *Engineering fracture mechanics*, 78(12):2369–2389, 2011.

[5] M. S. Chowdhury, C. Song, and W. Gao. Probabilistic fracture mechanics with uncertainty in crack size and orientation using the scaled boundary finite element method. *Computers & Structures*, 137: 93–103, 2014.

[6] J. A. Cottrell, T. J. Hughes, and Y. Bazilevs. *Isogeometric analysis: to-*

*ward integration of CAD and FEA*. John Wiley & Sons, 2009.

[7] S. M. Dsouza, T. M. Varghese, E. T. Ooi, S. Natarajan, and S. P. Bordas. Treatment of multiple input uncertainties using the scaled boundary finite element method. *Applied Mathematical Modelling*, 99:538–554, 2021.

[8] R. G. Ghanem and P. D. Spanos. *Stochastic finite elements: a spectral approach*. Courier Corporation, 2003.

[9] C. Jiang, X. Long, X. Han, Y. Tao, and J. Liu. Probability-interval hybrid reliability analysis for cracked structures existing epistemic uncertainty. *Engineering Fracture Mechanics*, 112:148–164, 2013.

[10] A. R. Khoei. *Extended finite element method: theory and applications*. John Wiley & Sons, 2015.

[11] C.-C. Li and A. Der Kiureghian. Optimal discretization of random fields. *Journal of engineering mechanics*, 119(6):1136–1154, 1993.

[12] X. Long, C. Jiang, X. Han, and W. Gao. Stochastic response analysis of the scaled boundary finite element method and application to probabilistic fracture mechanics. *Computers & Structures*, 153:185–200, 2015.

[13] S. Rahman. A galerkin isogeometric method for karhunen–loève approximation of random fields. *Computer Methods in Applied Mechanics and Engineering*, 338:533–561, 2018.

[14] C. Schwab and R. A. Todor. Karhunen–loève approximation of random fields by generalized fast multipole methods. *Journal of Computational Physics*, 217(1):100–122, 2006.

[15] C. Song and J. P. Wolf. The scaled boundary finite-element method—alias consistent infinitesimal finite-element cell method—for elastodynamics. *Computer Methods in applied mechanics and engineering*, 147(3-4):329–355, 1997.

[16] C. Song and J. P. Wolf. The scaled boundary finite-element method: analytical solution in frequency domain. *Computer Methods in Applied Mechanics and Engineering*, 164(1-2):249–264, 1998.

[17] B. Sudret and A. Der Kiureghian. *Stochastic finite element methods and reliability: a state-of-the-art report*. Department of Civil and Environmental Engineering, University of California . . . , 2000.

[18] P. Wriggers, F. Aldakheel, and B. Hudobivnik. *Virtual element methods in engineering sciences*. Springer, 2024.

[19] Q. Zang, J. Liu, W. Ye, F. Yang, R. Pang, and G. Lin. High-performance bending and buckling analyses of cylindrical shells resting on elastic foundation using isogeometric scaled boundary finite element method. *European Journal of Mechanics-A/Solids*, 100:105013, 2023.

[20] Z. Zheng and H. Dai. Simulation of multidimensional random fields by karhunen–loève expansion. *Computer Methods in Applied Mechanics and Engineering*, 324:221–247, 2017.